# Nano-scale surface wrinkling in chiral liquid crystals and plant-based plywoods

Pardis Rofouie,[a] Damiano Pasini[b] and Alejandro D. Rey*[a]

We present theoretical scaling and computational analysis of nanostructured free surfaces formed in chiral liquid crystals (LC) and plant-based twisted plywoods. A nemato-capillary model is used to derive a generalized equation that governs the shape of cholesteric free surfaces. It is shown that the shape equation includes three distinct contributions to the capillary pressure: area dilation, area rotation, and director curvature. To analyse the origin of periodic reliefs in plywood surfaces, these three pressure contributions and corresponding surface energies are systematically investigated. It is found that for weak homeotropic surface anchoring, the nano-wrinkling is driven by the director curvature pressure mechanism. Consequently, the model predicts that for a planar surface with a uniform tangential helix vector, no surface nano-scale wrinkling can be observed because the director curvature pressure is zero. Scaling is used to derive the explicit relation between the wrinkling's amplitude to the wavelength ratio as a function of the anisotropic surface tension, which is then validated with experimental values. These new findings can be used to characterize plant-based twisted plywoods, as well as to inspire the design of biomimetic chiro-optical devices.

## 1. Introduction

Biological liquid crystals (BLCs) are anisotropic viscoelastic materials exhibiting long-range orientational and partial positional order.[1] The liquid crystalline phase and topological defects in biological analogues are generally those of chiral nematics (cholesteric) phase, and hence are referred to as biological helicoidal plywoods,[2,3] also known as Bouligand architecture.[4] Helicoidal plywoods are found in many biological materials, such as DNA in human cells,[5] cellulose in plant cell walls,[6] chitin in arthropods cuticles,[2] and collagen in human compact bones.[7] BLCs are functional materials that display several unique properties,[8] such as nanoscale surface wrinkling observed in LC DNA,[9] cellulose,[10] and collagen.[11] Cholesteric films of concentrated collagen solutions exhibit periodic undulations at the free surface with an amplitude of the order of 150 nm, and a periodicity of the order of 3.5 μm.[11] Undulations of similar scales are also observed in silk gland ducts of the golden orb-web spider *Nephilaclavipes*,[12] the exoskeleton of the beetle *Chrysina gloriosa*,[13] and cellulosic materials.[10] These nano-scale structures that are spontaneously formed on the free surface of BLC are responsible for their particular optical responses resulting in structural colors, observed in beetles,[13] mollusk shells,[14] and few plants.[15] The study of the formation of these surface undulations is fundamental in understanding structural color in nature and can inspire the design of optical devices with novel functionalities.[16]

Photonic structures in many floral plants are associated with the shape and anatomy of plant surface topography. It has been reported that certain floral plant species, such as *Hibiscus trionum* and *Tulipakaufmanniana* petals, use ordered striation or ridges to obtain iridescence with a striking metallic appearance.[17] Although the formation of these micro- and nanostructures during the development of the petals is not yet well understood, it is believed that cellulosic CLCs are responsible for plant surface undulations and iridescent colors. In the preparation of a lyotropic cholesteric mesophase, Werbowyi and Gray discovered that concentrated aqueous solutions of (hydroxypropyl) cellulose (HPC) displayed iridescent colors that changed with concentration and viewing angle.[18] Efforts have been made to trap the CLC structure in solid films to create colored iridescent films.[19] Fernandes *et al.* fabricated iridescent solid cellulosic films with tunable mechanical and structural color properties, which mimic the structures found at the surface of the "Queen of the Night" tulip petals, which display periodic striation of about 1.5 μm, responsible for petal iridescence.[20] They indicated that the formation and periodicity of the surface structure are governed by the CLC structure.

Although the chiral surface structures are extensively studied by microscopy methods, including atomic force microscopy (AFM),[21] the complementary theoretical analysis of CLC surface wrinkling is rarely studied. The formation of surface nanostructures at CLC interfaces is a complex phenomenon

*[a]Department of Chemical Engineering, McGill University, 3610 University Street, Montreal, Quebec, H3A 2B2, Canada. E-mail: alejandro.rey@mcgill.ca; Fax: +1 514 398 6678; Tel: +1 514 398 4196*

*[b]Department of Mechanical Engineering, McGill University, Montreal, Quebec, H3A 2K6, Canada*

involving interfacial tension, surface anchoring energy, and LC Frank elasticity[8] that requires integrated multi-scale modelling of bulk and surface.[22] In a study of cholesteric liquid crystal free surface, Meister *et al.* described the periodic relief of a cholesteric liquid crystal interface by the minimisation of surface free energy composed of the anchoring energy and the surface tension.[23] They found that for relatively strong and finite anchoring, the surface deformation energy arises due to director surface gradient and elastic constants.[23a] The director distributions in the distorted region coupled with anchoring energy create nano-scale undulations at the free surface.

The plant cell wall is a multifunctional viscoelastic structure made of cellulose microfibrills (CMFs) coated with hemicelluloses and embedded in a matrix of lignin/pectin.[24] The plant cell wall includes a primary cell wall (p) laid down during growth on the outside and three secondary cell walls ($S_1$, $S_2$, $S_3$), which are formed when the cell has reached its final size and shape.[25] Although the primary and secondary wall layers differ in specific chemical composition (cellulose and hemicellulose contents are greater in secondary walls compared to primary walls) and structural organization (CMFs in primary layers are organized in a loose interwoven texture, whereas they are well oriented in secondary layers). Overall, CMFs in the polysaccharide matrix are oriented in strategic directions to form twisted plywood architecture for optimal mechanical efficiency. The proof that plant cell walls are formed through a liquid crystalline self-assembly process is the presence of the microstructure, textures and defect patterns observed in the secondary cell walls of some plant species.[8,26] The plant cell wall helicoidal plywoods can be characterized by the helical axis **H**, the pitch length $P_0$, which is the distance through which the fibers undergo a $2\pi$ rotation and handedness (sign of $P_0$), and the average fiber orientation **n**, which is normal to **H** (see Fig. 1).

In a recent communication[27] we briefly presented the main mechanism that operates in chiral capillarity using a plant-based plywood as a model material system. In this paper, we present a comprehensive analysis of the nanoscale structures observed at the chiral surfaces in detail and predict the response of the surface structure to chirality and anisotropic tension changes. We restrict our attention to the case in which the helical axis always remains parallel to the surface; other complex structures arising when the helical axis is tilted are beyond the scope of this paper. Focusing on the cellulosic CLCs material model, we use the generalized shape equation for anisotropic interfaces using the Cahn-Hoffman capillarity vector developed for LCs[28] and the well-known Rapini-Papoular anchoring energy[29] for the anisotropic part of the interfacial tension to analyze periodic nano-wrinkling in plant-based plywood free surfaces. The objective of this study is to identify the key mechanisms that induce and resist nano-wrinkling in CLCs and to formulate nano-wrinkling scaling laws of biomimetic utility for the design of optical gratings and as a tool to characterize plant-based plywoods.

This study is presented in the following manner: Section 2 presents the governing nemato capillary shape equation expressing the coupling mechanism between the surface geometry and cellulose fiber orientation for CLC/air interface in
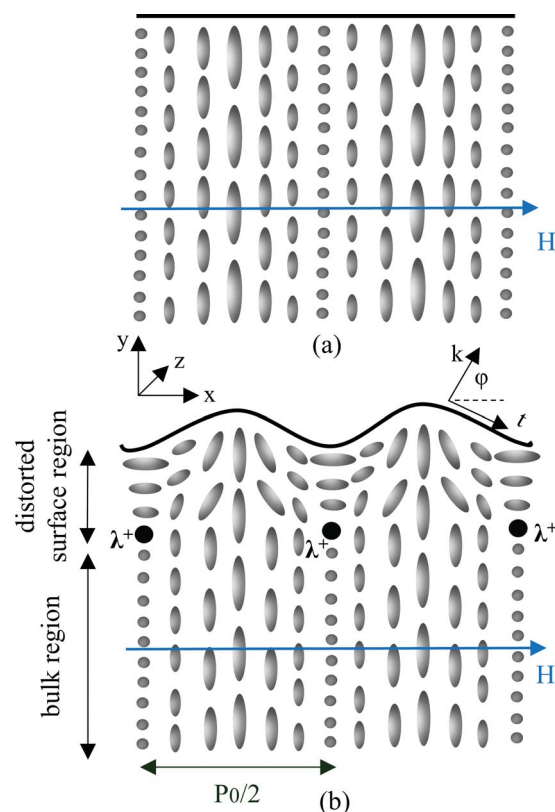


Fig. 1 Schematic of a cholesteric liquid crystal (plywood architecture) and surface structures. **H** is the helix unit vector, and $P_0$ is the pitch. (a) The surface director has an ideal cholesteric twist, and the surface is flat. (b) Bend and splay orientation distortions with $\lambda^+$ disclination[35] for $W < 0$ create surface undulations. Adapted from ref. 23a. Note that the director field is continuous everywhere, and $\lambda$ lines are non-singular core.

rectangular $(x, y, z)$ coordinates. The capillary shape equation is derived and described in terms of three capillary pressures. Appendix A presents the details of the derivation of the Cahn–Hoffman capillary vector thermodynamics for CLC interfaces. Appendix B derives the generic conditions, under which the director curvature pressure is zero. Appendix C formulates the capillary shape equation for the splay-bend director field relevant to nano-wrinkling. Section 3 analyses the effect of model parameters on the surface profile. The leading mechanism, which controls chiral wrinkling, is determined and the generic sufficient condition that results in flat and non-flat surfaces is derived. Furthermore, the surface energies associated with the CLC interface are presented and discussed. Finally, based on a standard order of magnitude analysis, a scaling formula expressing surface profile amplitude as a function of model parameters is presented and validated with a number of experimental biological CLC surface undulations and with numerical results. Section 4 presents the conclusions.

## 2. Capillary shape equation

We assume that the surface undulations in plant cell walls are formed through modulation in surface energy at the

anisotropic-air interface and are influenced by the macroscopic chirality of the cellulose fibers. The coupling mechanism between the surface geometry and cellulose fiber orientation can be demonstrated through the shape equation. In this section, the capillarity shape equation using the capillary vector $\xi$ (ref. 30) is presented for the CLC/air interfaces in rectangular $(x, y, z)$ coordinates, and the resulting surface pressures are formulated.

For isotropic interfaces, the capillary pressure, $p_c$, based on the well-known Young–Laplace equation, is proportional to the surface tension $\gamma$ and vanishes for plane surfaces ($\nabla_s \cdot \mathbf{k} = 0$):[31]

$$-p_c = -\nabla_s \cdot \mathbf{k}\gamma \tag{1}$$

where $\nabla_s = I_s \cdot \nabla$ is the surface gradient, $\mathbf{I}_s = \mathbf{I} - \mathbf{kk}$ is the $2 \times 2$ unit surface dyadic, and $\mathbf{k}$ is the surface unit normal. However, for a cholesteric liquid crystal (CLC) surface, the anisotropic surface tension contributes additional modes to the capillary pressure. The interfacial surface tension $\gamma$ for anisotropic surfaces is a function of the surface unit normal $\mathbf{k}$ and the director $\mathbf{n}$: $\gamma(\mathbf{k,n})$ and is given by Rapini and Papoular:[29]

$$\gamma(\mathbf{n}, \mathbf{k}) = \gamma_0 + \gamma_{aniso}(\mathbf{n}, \mathbf{k}); \quad \gamma_{aniso}(\mathbf{n}, \mathbf{k}) = \frac{W}{2}(\mathbf{n}.\mathbf{k})^2 \tag{2}$$

where $\gamma_0$ is the isotropic contribution, $\gamma_{aniso}$ is the anisotropic anchoring energy contribution, and $W$ is the anchoring energy coefficient. The anisotropic surface tension appears as the property that renormalizes the isotropic component of the interfacial tension and promotes the rotation of the interface. The anchoring energy contribution is associated with the director deviations from its preferred orientation due to bulk distortions or external fields. The preferred orientation or easy axis corresponding to eqn (2) can be parallel to the unit normal $\mathbf{k}$ (homeotropic) and perpendicular to the unit normal $\mathbf{k}$ (planar). In the present study, we restrict the discussion to homeotropic anchoring ($W < 0$) because for planar surface anchoring ($W > 0$, $\mathbf{n}\cdot\mathbf{k} = 0$), the helicoidal structure, in which the helical axis is perpendicular to the surface, will remain undistorted as it is the most stable and lowest energy state;[32] the undistorted helix results in a flat surface.[23a]

As the nematic director in CLCs continuously rotates along the helical axis, the helix structures (helixes perpendicular ($\mathbf{H}\cdot\mathbf{k} = 0$) and parallel ($\mathbf{H}\cdot\mathbf{k} = 1$) to the surface) for strong homeotropic anchoring ($W < 0$) are not fully compatible with any uniform aligning surface.[33] As a result, the average orientational order is disrupted due the frustration that leads to sub-surface defect nucleation, which can be resolved by changing the interface shape. The appearance of inclusions and the formation of defects in the bulk can change the director orientation in the CLC and results in a periodicity at the free surface whose wavelength can vary from half-helical pitch $P_0/2$ to $P_0$ or even greater.[21b,34] Herein, we assume that the pitch of the distorted region is equal to the bulk $P_0$. The effect of $\mathbf{n}(x)$ on the surface relief of the two CLC structures is shown in Fig. 1. The distorted surface layer can be generated either by vertical or tangential helixes in the bulk (note that only a horizontal helix alignment $\mathbf{H}$ is presented in Fig. 1).

The Cahn–Hoffman capillary vector $\xi$ (ref. 30) is the fundamental quantity that provides a direct and clear method to explain the role of anisotropy in capillary pressure and its role in surface shape determination. The capillary vector $\xi$ takes into account the changes in surface energy due to surface dilation (change in area) and surface rotation (change in unit normal $\mathbf{k}$) in one single vectorial quantity. In this section, the key formulations of capillary vector thermodynamics are presented. Appendix A gives the details of the derivation of the Cahn–Hoffman capillary vector thermodynamics for anisotropic interfaces.[28] The capillary vector $\xi$ for nematic surfaces and interfaces has two components:

$$\xi(\mathbf{n}, \mathbf{k}) = \xi_\perp(\mathbf{n}, \kappa) + \xi_\parallel(\mathbf{n}, \mathbf{k})$$
$$\xi_\perp(\mathbf{n}, \mathbf{k}) = \gamma\mathbf{k}; \xi_\parallel(\mathbf{n}, \mathbf{k}) = \mathbf{I}_s \cdot \frac{d\gamma}{d\mathbf{k}} \tag{3}$$

The normal component $\xi_\perp$ describes the increase in surface energy through dilation, and the tangential component $\xi_\parallel$ is the change in surface energy through rotation of the unit normal. For isotropic surfaces, $\xi_\parallel = 0$ and no rotational effects appear because $W = 0$. It is important to note that at the free surface, we have two independent fields: the director $\mathbf{n}$ and the unit normal $\mathbf{k}$. A soft surface describes the case in which its shape adapts to a given director orientation, as considered in this paper.

The normal component of the interfacial stress boundary conditions at the CLC/air interface is

$$-\mathbf{kk}:(\mathbf{T}^a - \mathbf{T}^b) = (\nabla_s \cdot \mathbf{T}_s)\cdot\mathbf{k}, \tag{4}$$

where $\mathbf{T}^{a/b}$ is the total stress tensor in the air and cholesteric bulk phase, and $\mathbf{T}_s$ is the interface stress tensor. The air and bulk stress tensors are expressed as

$$\mathbf{T}^a = -p^a\mathbf{I}$$

and

$$\mathbf{T}^b = -(p^b - f_b)\mathbf{I} + \mathbf{T}^E; \mathbf{T}^E = -\frac{\partial f_b}{\partial \nabla\mathbf{n}}\cdot(\nabla\mathbf{n})^T, \text{ respectively,} \tag{5}$$

where $p^{a/b}$ are the hydrostatic pressures, $f_b$ is the bulk Frank energy density, and $\mathbf{T}^E$ is the Ericksen stress tensor. The projection of eqn (4) along $\mathbf{k}$ results in the shape equation

$$\underbrace{(p^a - p^b) + (f_b) - \mathbf{kk}:\left(\frac{\partial f_b}{\partial \nabla\mathbf{n}}\cdot(\nabla\mathbf{n})^T\right)}_{\text{bulk normal stress jump, SJ}} = \underbrace{(\nabla_s\cdot\mathbf{T}_s)\cdot\mathbf{k}}_{-\text{capillary pressure, } -p_c} \tag{6}$$

where SJ is the total normal stress jump, and $p_c$ is the capillary pressure. The bulk free energy density of a cholesteric in the one constant approximation reads

$$f_b = \frac{1}{2}K\left((\nabla\cdot\mathbf{n})^2 + (\mathbf{n}\cdot\nabla\times\mathbf{n} - q_0)^2 + (\mathbf{n}\times\nabla\times\mathbf{n})^2\right), \tag{7}$$

where $K$ is the Frank elasticity constant, and $q_0$ is the wave vector, which is equal to $2\pi/P_0$. The surface contribution $(\nabla_s\cdot\mathbf{T}_s)\cdot\mathbf{k}$ is minus the divergence of the capillary vector naturally decomposed as[36]

$$-p_c = (\nabla_s \cdot \mathbf{T}_s) \cdot \mathbf{k} = -\nabla_s \cdot \boldsymbol{\xi} = -\nabla_s \cdot (\boldsymbol{\xi}_\parallel + \boldsymbol{\xi}_\perp)$$

$$= - \underbrace{\frac{\partial \boldsymbol{\xi}_\perp}{\partial \mathbf{k}} : \nabla_s \mathbf{k}}_{\substack{P_{\text{dilation}} \\ \text{(area size change)}}} - \underbrace{\frac{\partial \boldsymbol{\xi}_\parallel}{\partial \mathbf{k}} : \nabla_s \mathbf{k}}_{\substack{P_{\text{rotation}} \\ \text{(area rotation)}}} - \underbrace{\frac{\partial \boldsymbol{\xi}_\parallel}{\partial \mathbf{n}} : \nabla_s \mathbf{n}}_{\substack{P_{\text{director}} \\ \text{(director curvature)}}},$$

$$(8)$$

where $P_{\text{dilation}}$ is the contribution from the normal component $\boldsymbol{\xi}_\perp$, which is the usual Laplace pressure, and $P_{\text{rotation}}$ is the contribution from the tangential component $\boldsymbol{\xi}_\parallel$. This is the anisotropic pressure due to preferred orientation and is known as Herring's pressure. The additional contribution to the capillary pressure, $P_{\text{director}}$ appears from director curvature due to orientation gradients. The capillary pressure in CLC-free interfaces includes a number of novel interfacial effects: (i) capillary pressure even for flat surfaces, (ii) Laplace-type capillary pressure due to director orientation curvature (i.e. gradients), and (iii) orientation-dependent renormalization of the surface tension coefficients due to anchoring energy.[28]

For the case under consideration, in the absence of gravitation, semi-infinite media in the vertical direction and periodic in the horizontal direction, we take $p^a - p^b = 0$. The remaining contribution to SJ, $\{f_b + \mathbf{kk}:\mathbf{T}^E\}$, is known as the elastic correction in the liquid crystal literature. Using eqn (6) and (7), the elastic correction is

$$\text{SJ} = \left\{ f_b + \mathbf{kk} : \mathbf{T}^E \right\}$$

$$= \frac{1}{2} K \left( (\nabla \cdot \mathbf{n})^2 + (\mathbf{n} \cdot \nabla \times \mathbf{n} - q_0)^2 + (\mathbf{n} \times \nabla \times \mathbf{n})^2 \right)$$

$$- K(\mathbf{n} \cdot \nabla \times \mathbf{n} - q)(\mathbf{n} \cdot (((\mathbf{k} \cdot \nabla)\mathbf{n}) \times \mathbf{k}))$$

$$- K((\mathbf{n} \cdot \nabla \mathbf{n})(\mathbf{n} \cdot \mathbf{k})) \cdot ((\mathbf{k} \cdot \nabla)\mathbf{n}) - K(\nabla \cdot \mathbf{n})((\mathbf{k} \cdot \nabla)\mathbf{n}) \cdot \mathbf{k} \quad (9)$$

This expression can be greatly simplified. Using the director field of ref. 23a, with $\mathbf{n} = (n_x(x,y),\ n_y(x),\ n_z(x,y))$ and the interfacial torque balance equation, we find that the Ericksen stress projection is zero:

$$\mathbf{kk} : \mathbf{T}^E = \left( \left( (\mathbf{I} - \mathbf{nn}) \cdot \frac{\partial \gamma}{\partial \mathbf{n}} \right) \cdot (\nabla \mathbf{n})^T \right) \cdot \mathbf{k} = 0 \quad (10)$$

because $\partial n_y / \partial y = 0$. The elastic correction SJ in the present case is then only due to $f_b$. Using eqn (6), (9) and (10) and $\mathbf{n} = (n_x(x,y), n_y(x), n_z(x,y))$ we obtain[37]

$$\frac{Kq_0^2}{2}\left(1 + n_{y}^2\right) = \left(\gamma_0 - \frac{W}{2}(\mathbf{n}\cdot\mathbf{k})^2 + W(\mathbf{n}\cdot\mathbf{t})^2\right)\kappa$$

$$- W\left\{ (\mathbf{k}\cdot\mathbf{n})\left(\mathbf{t}\frac{d\mathbf{n}}{ds}\right) + \mathbf{kn} : \left(\mathbf{t}\frac{d\mathbf{n}}{ds}\right) \right\} \quad (11)$$

where $\kappa = d\varphi/ds$ is the surface curvature, $\varphi$ is the normal angle, $s$ is the arc-length (Appendix C, Fig. 10) and $\mathbf{t}$ is the tangential surface unit vector. For significant anchoring that unravels the helix, we find that the extrapolation length $\ell_{\text{ex}}$ scales as

$$\ell_{\text{ex}} = \frac{K}{W} = cP_0 \quad (12)$$

where $c$ is the ratio of the extrapolation length $K/W$ to the cholesteric pitch $P_0$. Thus, the order of magnitude of the stress jump (elastic correction) written in relation to anchoring (i.e. $W/P_0$) gives

$$\text{o}(\text{SJ}) = \text{o}\left(\frac{K}{P_0^2}\right) = \text{o}\left(W\frac{K}{WP_0^2}\right) = \text{o}\left(W\frac{\ell_{\text{ex}}}{P_0^2}\right) = \text{o}\left(c\frac{W}{P_0}\right) \quad (13)$$

For typical cholesteric liquid crystals, the internal length $K/\gamma_0$ is usually in the range 1 nm (an order of magnitude estimation of the elastic constant $K$, and the surface tension $\gamma_0$ gives $K \approx 10^{-11}$ J m$^{-1}$ and $\gamma_0 \approx 10^{-2}$ J m$^{-2}$). As the ratio of $W/\gamma_0$ at the cholesteric-air interface with quite strong anchoring lies in the range ($B = W/\gamma_0 = 0.05$), the extrapolation length scale $K/W$ is about

$$\frac{K}{W} = \frac{K/\gamma_0}{W/\gamma_0} \sim \frac{1\ [\text{nm}]}{0.05} \sim 20\ [\text{nm}] \quad (14)$$

With these values, for a biological cholesteric liquid crystal with a typical pitch $P_0 \sim 1$ μm, the value of $c$ is in the order of $\frac{K/W}{P_0} = \frac{20\ [\text{nm}]}{1000\ [\text{nm}]} = 0.02$. Hence, if $c$ is of the order of 0.02, the SJ contributes 2% to the shape equation, and the elastic correction to the surface shape is not significant and can be neglected to describe nano-scale surface undulations. When $P_0$ increases beyond 1 μm, the elastic correction essentially vanishes. When the elastic correction is essentially negligible, the shape eqn (11) reduces to a balance of dilation, rotation, and director pressures when the director field and geometry are as shown in Fig. (1):

$$\underbrace{\left(1 - \frac{B}{2}(\mathbf{n}\cdot\mathbf{k})^2 + B(\mathbf{n}\cdot\mathbf{t})^2\right)\kappa}_{P_{\text{dilation}} + P_{\text{rotation}}} \underbrace{- B\{(\mathbf{k}\cdot\mathbf{n})(\nabla_s \cdot \mathbf{n}) + \mathbf{kn} : \nabla_s\mathbf{n}\}}_{P_{\text{director}}} = 0,$$

$$(15)$$

where $B = W/\gamma_0$ is the scaled anchoring coefficient. This equation shows that the surface shape is the balance between surface tension and anchoring. The anchoring term is the driving force for surface undulations, and it originates from the fact that this anisotropic surface energy is minimized when the director $\mathbf{n}$ is aligned along the preferred "easy axis". For a fixed cholesteric helical orientation, the only method to minimize this energy is to deform the interface to avoid an energetically costly mismatch between the director and the easy axis. Because the director of a cholesteric is periodic, the surface undulations are also periodic. When the director orientation deviates from the easy axis and the deviation generates gradients in surface tension, which are comparable to the characteristic kinetic energy density, the orientational-driven Marangoni flow may appear.[38] In this paper, we neglect this Marangoni effect and consider the shape instability as driven by elastic effects. One mechanism that may eliminate or reduce viscous effects when the helix is tangential to the surface is the high viscosity associated with permeation flow.[39]

For flat planar interfaces ($\kappa = 0$), the capillary pressure is driven only by director curvature:

$$p_c = W((\mathbf{k}\cdot\mathbf{n})(\nabla_s\cdot\mathbf{n}) + \mathbf{kn}:\nabla_s\mathbf{n}) \qquad (16)$$

The director curvature pressure, $P_{director}$ is zero when

$$(\mathbf{k}\cdot\mathbf{n})(\nabla_s\cdot\mathbf{n}) + \mathbf{kn}:\nabla_s\mathbf{n}) = 0 \rightarrow \nabla_s\cdot\mathbf{n} = 0 \text{ and } \mathbf{kn}:\nabla_s\mathbf{n} = 0 \qquad (17)$$

In a rectangular $(x, y, z)$ coordinate system, to satisfy the zero director curvature pressure condition (17), we find that the director $\mathbf{n}$ must obey one of the following two conditions: (1) $n_x = 0$ and ($n_y = 0$ or 2) $n_x n_y = $ constant (the generic conditions under which the director curvature pressure is zero are derived in Appendix B). We note that the surface director field describing a planar surface with a uniform tangential helix vector is given by $\mathbf{n}(x) = (0, \cos qx, \sin qx)$, and because $n_x = 0$, the director curvature pressure is zero and no surface wrinkling can be observed, as previously predicted using other approaches.[23a]

To describe 1D surface undulation in a CLC, we use a rectangular coordinate frame $(x, y, z)$, where $x$ is the undulation direction, and $y$ the vertical axis (see Fig. 1). The amplitude of the vertical undulation is $h(x)$. For a 1D texture, the surface relief is constant in the $z$ direction. The arc-length measure of the undulating surface is "$s$".

$$\frac{d\varphi}{dx} = \frac{p_c + q_0 B \sin(\varphi)\left\{\sin^2(\varphi - q_0 x) - \cos^2(\varphi - q_0 x)\right\}}{\sin(\varphi)\left\{1 - \dfrac{B}{2}\cos^2(\varphi - q_0 x) + B\sin^2(\varphi - q_0 x)\right\}} \qquad (18)$$

Setting $p_c = 0$ and using the previously specified splay-bend director $\mathbf{n}(x) = (\cos qx, \sin qx, 0)$ and surface unit normal $\mathbf{k}(x)$ vectors gives the governing nonlinear first-order ODE for the normal angle $\varphi(x,B,P_0)$, where $-2 < B < 0$, $0 < P_0 < 100$ μm, $0 < x < L$, where $L$ is the given system length in the $x$ direction. This nonlinear ODE with periodic coefficients is solved using the well-known AUTO nonlinear software.[40] The surface relief is then obtained from $h(x) = \int_0^x \cot\varphi \, dx'$. The boundary condition at $x = 0$, is $\varphi|_{x=0} = \dfrac{\pi}{2}$, consistent with the adopted sign of B.

# 3. Results and discussion

In this section, we (1) establish and quantify the effect of anchoring (B) and chirality ($P_0$) on the normal angle $\varphi(x,B,P_0)$ and on the amplitude profile $h(x,B,P_0)$, (2) use a pressure-energy analysis to characterize wrinkling, and (3) formulate and validate scaling relations for $h_{max}$ as a function of $B$ and $P_0$.

## 3.1. Free surface profile

The generic features of the amplitude profile $h(x)$, its maximum value $h_{max}$, and its periodicity $h(x) = h(x + \lambda)$ are the three relevant outputs of the model. The two significant parameters

influencing $h(x)$ are the scaled anchoring coefficient $B$ and the micron scale length of the pitch $P_0$. For the nematic-isotropic interface, the scaled anchoring coefficient $B$ is of the order of magnitude 0.01.[41] The anchoring strength $W$ at the nematic-air interface is about several orders of magnitude larger compared to the anchoring strength at the nematic-isotropic interface. However, as the surface tension at the nematic-air interface is higher than the surface tension at the nematic-isotropic interface,[23a,42] the scaled anchoring coefficient $B = W/\gamma$ is taken to be in the range $-0.1 < B < -0.01$.

The plots of the normal angle $\varphi(x)$ and corresponding surface reliefs $h(x)$ as a function of the distance "$x$", for different $B$ and $P_0$ are shown in Fig. 2 and 3, respectively. As expected, in the periodicity, $\lambda$ equals the pitch, and $P_0$ and the amplitude are in the nanometer range, which is consistent with experimental findings.[21a,43] Increasing both the parameters of $B$ and $P_0$ results in higher amplitudes.

## 3.2. Pressure–curvature relations

Because at the nematic-air interface, the anchoring strength ($W \approx 10^{-5}$ J m$^{-2}$) is three orders of magnitude smaller than the surface tension ($\gamma \approx 10^{-2}$ J m$^{-2}$),[30] it would seem that there is no driving forces to deform the CLC-free interfaces and a flat interface would minimize the free surface energy. However, the director pressure curvature is herein shown to be a driving force that wrinkles the surface under weak anchoring (i.e. small B) and typical values of chirality (i.e. $P_0$ in the μm range). All pressures are scaled with the isotropic tension $\gamma_0$ and have units of μm$^{-1}$. Due to the orientational order of CLC interface, the
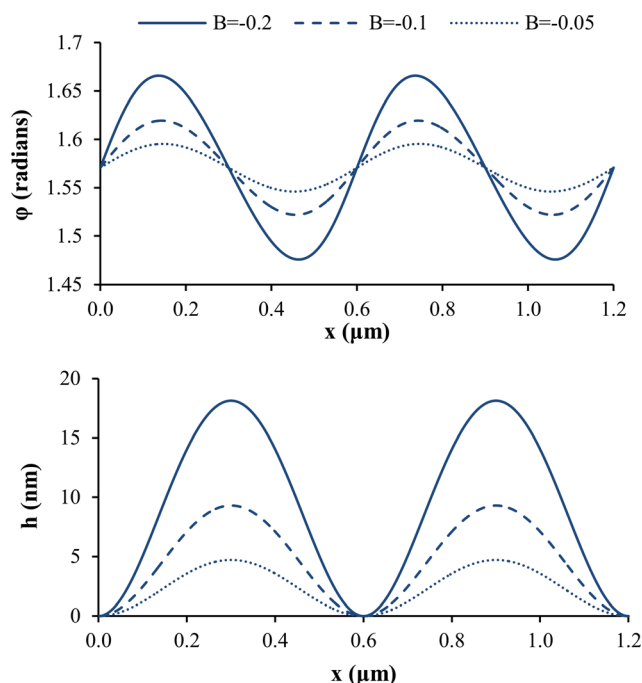


Fig. 2 The numerical solutions $\varphi(x)$ and $h(x)$ for $P_0 = 1.2$ μm and different values of $B = -0.05, -0.1$, and $-0.2$, showing the increase of the normal angle $\varphi$ and the resultant surface amplitude $h$ through an increase in the anchoring constant $B$.
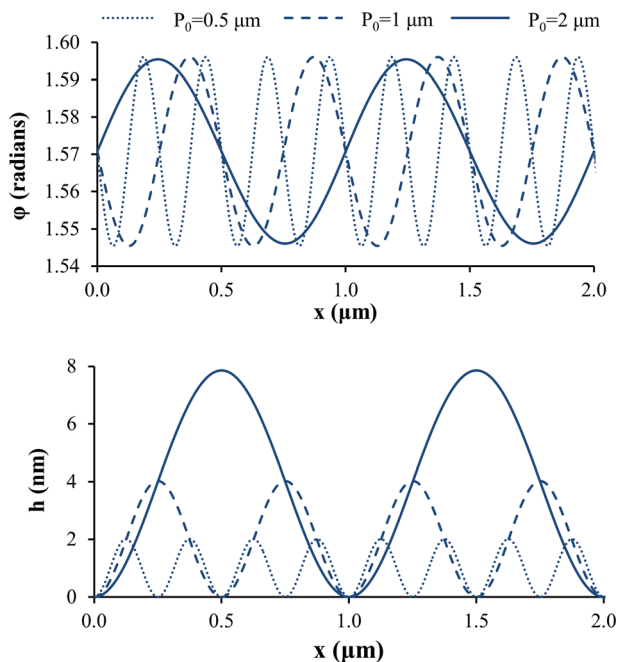
Fig. 3 The numerical solutions $\varphi(x)$ and $h(x)$ for $B = -0.05$ and different values of $P_0 = 0.5$, 1 and 2 μm, showing the increase of the normal angle $\varphi$ and the resultant surface amplitude $h$ by an increase in the helical pitch $P_0$.

capillary pressure contains three contributions: surface area reduction, surface area rotation, and director curvature (eqn (8)). The essential feature of chiral capillarity is the interaction of anisotropy (director **n** of fibers), micron-range chirality ($P_0$), helix direction (**H**) and free-surface topography. When the cholesteric helix is parallel to a flat surface, frustration caused by the unavoidable (due to periodic **n**) presence of high surface energy allows the surface uncoiling of the helix and the periodic tilting of the interface. This is another example of pattern

formation by disturbance, which is ubiquitous in mesophases.[8,44]

A unique feature of liquid crystal surfaces[28] is the presence of Laplace pressure (area dilation), Herring's pressure (area rotation), and director orientation gradients pressure, as revealed succinctly by the surface gradient of the capillary vector ξ (eqn (15)). Herring's pressure forms the basis of anisotropic crystal morphologies[28] and is included here as $P_{\text{rotation}}$. As the Herring's pressure depends on curvature, it is only the orientation pressure $P_{\text{director}}$ that wrinkles the surface with a wavelength that reflects the periodicity of the director field. Extracting the curvature in eqn (15) clearly shows that it is the ratio of a wrinkling driving force $(-P_{\text{director}})$ to a resistance to wrinkling (capillary tension coefficients):

$$\kappa = \frac{\text{driving force}}{\text{resistance}} = \frac{-P_{\text{director}}}{\left(\gamma + \dfrac{\partial^2 \gamma}{\partial s^2}\right)} = \frac{B\big((\mathbf{k}\cdot\mathbf{n})(\nabla_s\cdot\mathbf{n}) + \mathbf{kn} : \nabla_s\mathbf{n}\big)}{1 - B\left(\dfrac{1}{2}(\mathbf{n}\cdot\mathbf{k})^2 + (\mathbf{n}\cdot\mathbf{t})^2\right)},$$

(19)

where the capillary tension coefficients are the usual Laplace terms plus the Herring's coefficient[28] given by the second derivative $\dfrac{\partial^2 \gamma}{\partial \mathbf{k}^2} = \mathbf{tt} : \left(\partial\left(\mathbf{tt}\cdot\dfrac{\partial \gamma}{\partial \mathbf{k}}\right)\partial\mathbf{k}\right)$; the last ratio is obtained by scaling with $\gamma_0$. Clearly, as $P_{\text{director}} = 0 \rightarrow \kappa = 0$ (see also Appendix C).

This is illustrated in Fig. 4 through 3-D representation of the surface curvature, $\kappa$, and associated pressure directors, $P_{\text{director}}$, and normal angle, $\varphi$, for two anchoring coefficients and three chirality values. Fig. 4 shows that for all values of the anchoring coefficients and chiralities, the zero-pressure director results in a flat surface (zero curvature). The horizontal diameter corresponds to the zero-pressure director ($P_{\text{director}} = 0$). Using scaling arguments, the $P_{\text{director}}$ scales as

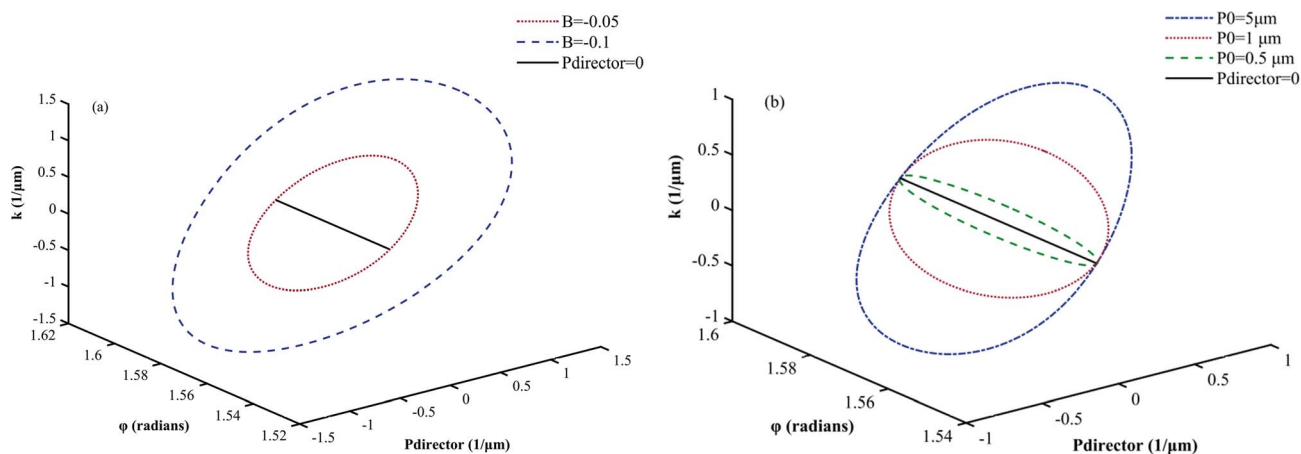$$P_{\text{director}} = \text{order}\left(\frac{B}{P_0}\right).$$

(20)



Fig. 4 3-D representation of the surface curvature and associated pressure directors $P_{\text{director}}$ and normal angle $\varphi$. (a) $P_0 = 0.5$ μm, $B = -0.05$, $-0.1$; and (b) $B = -0.05$, $P_0 = 0.5$, 1, and 5 μm, showing the increase in the maximum curvature for higher values of $B$ and lower values of $P_0$. The diameter corresponds to the zero-pressure director ($P_{\text{director}} = 0$).
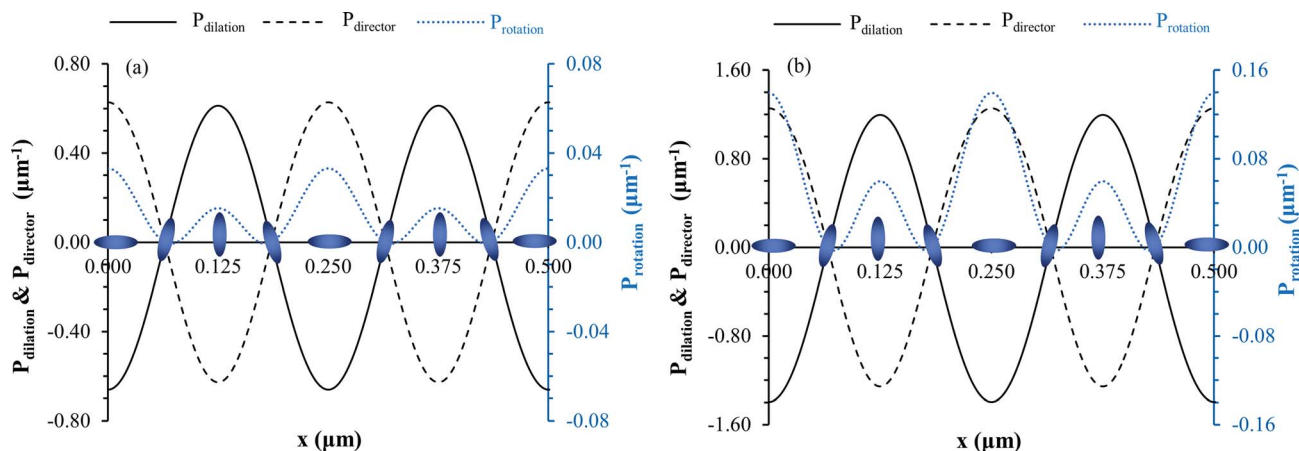
**Fig. 5** Pressure profiles for $P_{dilation}$, $P_{rotation}$ and $P_{director}$ as a function of distance "$x$": (a) $B = -0.05$ and $P_0 = 0.5$ μm and (b) $B = -0.1$ and $P_0 = 0.5$ μm. The ellipsoid corresponds to the director orientation. The figures display that pressure extrema occur at planar and homeotropic orientation. When the director angle is $\pi/4 < \theta < \pi/2$, dilation and rotation are in-phase and when $0 < \theta < \pi/4$, rotation and director curvature are in-phase. Dilation and director curvature pressures are always out-of-phase.

Therefore, from eqn (19) and (20) we see that the maximum curvature will increase with $B$ and decrease with $P_0$, in agreement with the computations. This dependence is manifested in the 3-D plots of the surface curvature for different anchoring coefficients ($B = -0.05$, and $-0.1$) and chirality ($P_0 = 0.5$, 1, and 5 μm), as shown in Fig. 4a and b, respectively.

Fig. 5 shows the three scaled surface pressures as a function of "$x$" for two anchoring coefficients and $P_0 = 0.5$ μm. The ellipsoids correspond to the director orientation. Pressure extrema (and surface relief extrema as in Fig. 2 and 3) occur at planar and homeotropic orientation. The Herring's pressure $P_{rotation}$ is always positive and alternates its phase along each cycle, such that when the director angle is $\pi/4 < \theta < \pi/2$, dilation and rotation are in-phase and when $0 < \theta < \pi/4$, rotation and director curvature are in-phase. Note that dilation and director curvature pressures are always out-of-phase. In addition, its amplitude also oscillates. Increasing the anchoring strength increases the magnitude of all pressures. The polar plots of the three scaled capillary pressures as a function of anchoring $B$ and chirality $P_0$, are shown in Fig. 6 and 7, respectively. The angular coordinate is the director field $\theta$. The fourfold symmetry reflects the facts that the pressure extrema are at 0, $n\pi/2$; $n = \{\pm1,2,...\}$ and that all pressures vanish at $n\pi/4$; $n = \{\pm1,3...\}$. The figure shows that pressure asymmetry is strongest for the chiral component $P_{rotation}$, but is essentially zero for the other two. Fig. 7 shows polar plots of pressure as a function of $P_0$. Decreasing chirality decreases all pressures as the wavelength of the undulation increases. Changing $P_0$ does not
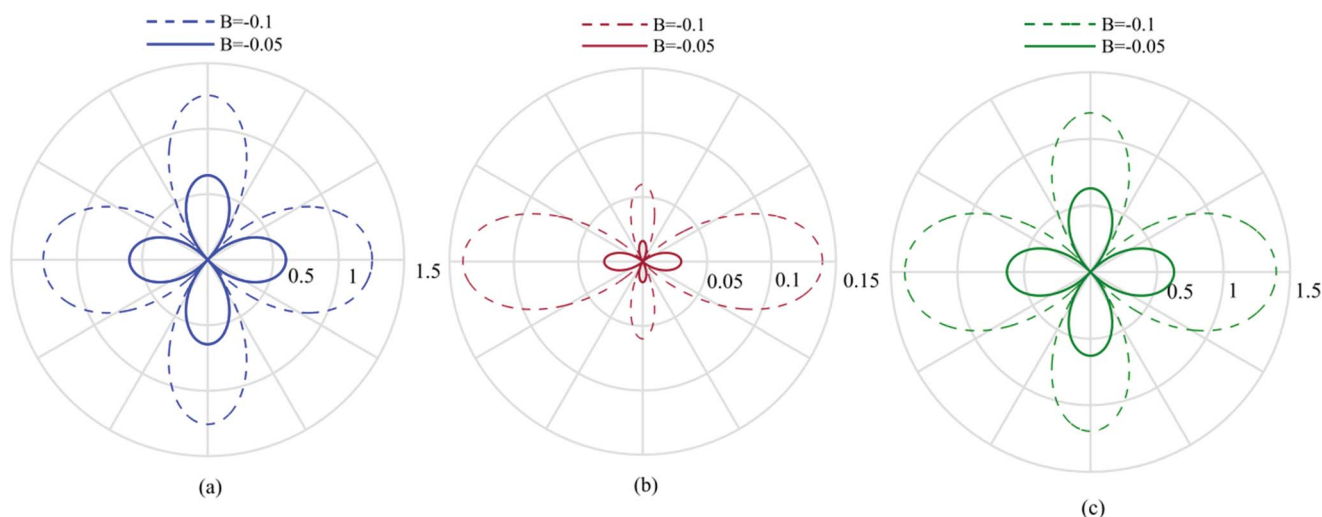


**Fig. 6** Polar plots of the three scaled capillary pressures: (a) $P_{dilation}$ (μm$^{-1}$), (b) $P_{rotation}$ (μm$^{-1}$), (c) $P_{director}$ (μm$^{-1}$) for $B = -0.05$ and $-0.1$, and $P_0 = 0.5$ μm. The angular coordinate is the director field $\theta$. The fourfold symmetry reflects the facts that the pressure extrema are at 0, $n\pi/2$; $n = \{\pm1,2,...\}$ and that all pressures vanish at $n\pi/4$; $n = \{\pm1,3...\}$.

**Fig. 7** Polar plots of the three scaled capillary pressures: (a) $P_{\text{dilation}}$ ($\mu m^{-1}$), (b) $P_{\text{rotation}}$ ($\mu m^{-1}$), (c) $P_{\text{director}}$ ($\mu m^{-1}$) for $P_0 = 0.5$ & 1 $\mu m$ and $B = -0.5$. The fourfold symmetry reflects the facts that the pressure extrema are at 0, $n\pi/2$; $n = \{\pm1,2,\ldots\}$ and that all pressures vanish at $n\pi/4$; $n = \{\pm1,3\ldots\}$.
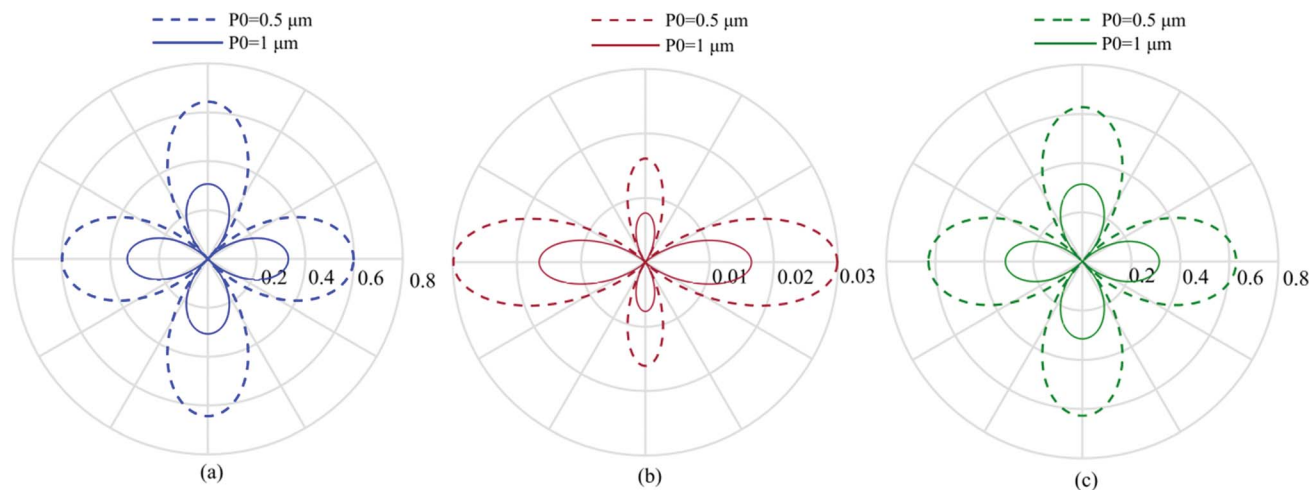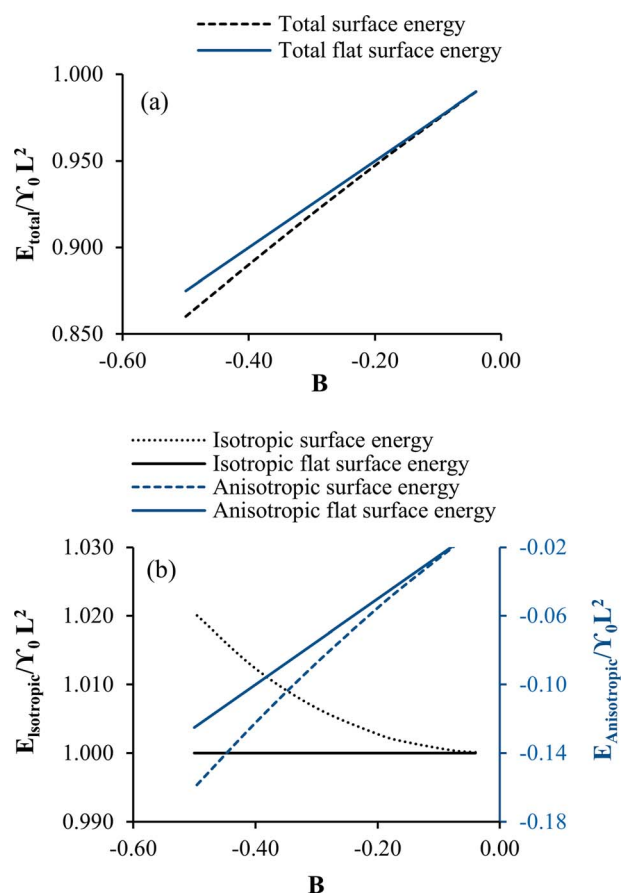


**Fig. 8** (a) The total surface energy and (b) isotropic and anisotropic contributions compared with flat surface energies for $P_0 = 0.5$ $\mu m$ and different values of $B = -0.5$ to $-0.05$. The system reduces its free energy by decreasing its anisotropic surface energy.

### 3.3. CLC surface energies

The total surface energy is defined by $F_{\text{s}} = \int \gamma dA$,[45] and for an initially flat surface of area $L^2$, the total scaled surface energy $\varepsilon_{\text{T}}/\gamma_0 L^2$ is

$$\frac{\varepsilon_{\text{T}}}{\gamma_0 L^2} = \underbrace{\frac{1}{L^2} \int_0^L \int_0^L \frac{1}{\sin \varphi} dx dz}_{\text{isotropic surface tension}} + \underbrace{\frac{B}{L^2} \int_0^L \int_0^L (\mathbf{n} \cdot \mathbf{k})^2 \frac{1}{\sin \varphi} dx dz}_{\text{anchoring energy}} . \quad (21)$$

Fig. 8 shows the variations of the total surface energy with the two surface energy contributions for various $B$ in comparison with the flat surface energy contributions. Fig. 8a shows the total scaled surface energy of the wrinkled and flat surfaces as a function of anchoring $B$. Increasing the magnitude of $B$ increases the energy difference between the flat and undulating surfaces. The figure demonstrates that the total energy monotonically decreases by increasing the magnitude of $B$. Fig. 8b shows the different contributions of the profiles shown in Fig. 8a. The undulation is driven by the anisotropic surface energy despite the increase in the isotropic energy. In addition, the decrease in anisotropic energy is significantly augmented by the undulations.

Fig. 9 shows the corresponding energy contributions and behaviour as a function of chirality. The figure shows that the isotropic surface tension energy and the anchoring energy for a particular value of anchoring ($B = -0.05$) are almost independent of chirality. Although the undulating surface has a higher isotropic energy, compared with the flat surface, the lower anisotropic energy yields the undulating surface with a lower total surface energy, compared with the flat surface reference line (Fig. 9a).

### 3.4. Undulation scaling law and validation

Using a standard order of magnitude analysis based on eqn (8), we find a revealing close-form expression for the maximum amplitude $h_{\text{max}}$ as a function of $B$ and $P_0$:

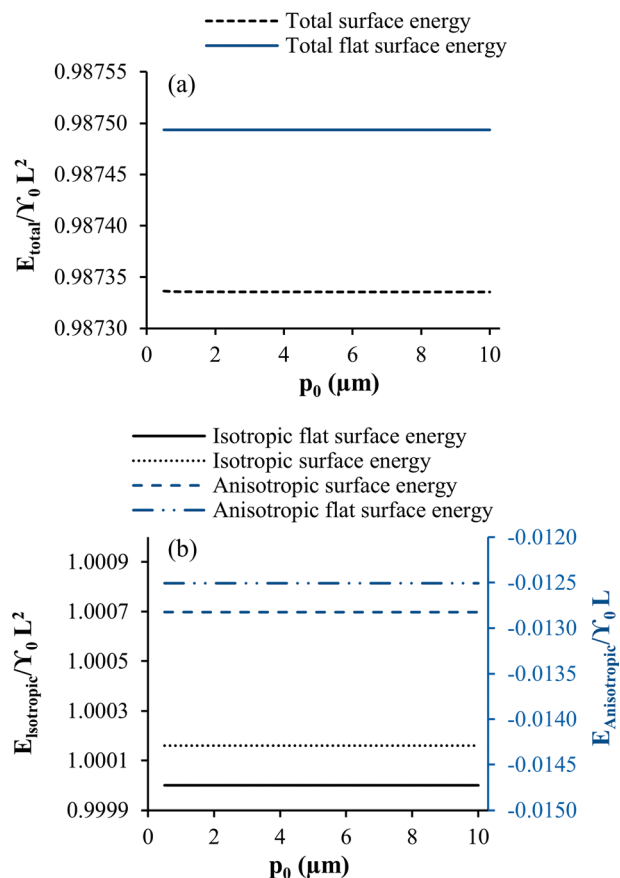affect the degree of asymmetry between the lobes of these pressures.

Fig. 9 (a) The total surface energy and (b) isotropic and anisotropic contributions compared with flat surface energies for $B = -0.05$ and different values of $P_0 = 0.5$ μm to 10 μm, showing that the system free energy is almost insensitive to the variations of helix pitch $P_0$.

Table 1 Validation of the scaling law eqn (22) with experimentally observed nano-scale surface undulations in CLCs and biological plywoods

| Experiments | $h$ (nm) | $\lambda$ (μm) | $B^{\text{fitted}}$ |
|---|---|---|---|
| Chiral polymer[21a] | 2.5 | 0.63 | 0.028 |
| Collagen solution[46] | 100 | 7.5 | 0.079 |
| Liquid crystalline collagen[11] | 150 | 8 | 0.110 |
| Cellulosic cholesteric film[20] | 5 | 0.5 | 0.059 |

$$h_{\max} = \frac{BP_0}{1 + \delta B}. \tag{22}$$

The numerical results indicate that $\delta = 10.71B^{-1.02}$. The prediction is that the ratio of amplitude/periodicity is essentially a linear function of the scaled anchoring $B$:

$$\frac{h_{\max}}{P_0} = 0.085B.$$

Because the value of $B$ for the interface between the chiral nematic and the isotropic phase/air is usually in the range $-0.1 < B < -0.01$, the estimated amplitude of surface undulation is about one percent of the undulation wavelength. The theoretical estimate, based on the shape equation, of the depth-to-

period ratio is consistent with the nano-scale surface structures that have been experimentally observed in a variety of polymeric and biological CLC. Periodic surface structures with amplitude of the order of hundreds of nanometers and a periodicity of the order of a few micrometers that spontaneously appeared from evaporating droplets of collagen solutions on glass substrates were detected using atomic force microscopy (AFM).[45] The periodic surface relief found in this work is very similar to the periodic undulations observed in a collagen film with twisted plywood architecture.[11] In addition, the AFM images of sheared nanocrystalline cellulose thin films showed two periodic gratings with different scales: the primary periodic structure perpendicular to the shear direction and a smoother texture characterized by a secondary periodic structure, which is very similar to the surface modulation found in the Tulip "Queen of the Night" petals.[20] The estimated values of the parameter B for several surface nano-undulations of CLC (ref. 11, 20, 21 and 46) are shown in Table 1. The results show that the predicted values of parameter $B$ using the scaling law are consistent with the anchoring energy coefficients for the CLC/air interface.

## 4. Conclusions

This paper has used a non-linear nemato-capillarity shape equation to describe the main mechanisms driving nano-scale surface undulations in chiral nematic liquid crystals as shown in plant-based plywoods and various cholesteric liquid crystals. The generalized Laplace equation based on the Cahn–Hoffman capillarity vector formalism was formulated and used as an efficient tool to analyse surface reliefs in plant-based plywoods. The resulting chiral capillary equation admits stable, spatially periodic solutions describing surface wrinkling, in which the amplitude is in the order of few nms and the wavelength is in the order of μms. The role of three capillary pressure contributions (surface area change, surface area rotation, and director curvature) have been elucidated, and the influence of chirality and surface anchoring has been characterized. The director pressure has been identified as the fundamental driving force that generates the surface nano-scale undulations. The model predictions show that the director pressure vanishes for a planar surface with a uniform tangential helix vector and results in a flat surface. A scaling law for the chirality-driven surface wrinkling shows that the ratio of amplitude-to-period is a linear function of the ratio of anchoring strength to isotropic surface tension ($0.085 \times W/\gamma_0$). The scaling law is validated with experimental values available in literature for surface undulations observed in CLCs and biological plywoods. Because the pitch $P_0$ of cholesteric liquid crystals and plywoods is sensitive to temperature, water content, pH, and external fields, we expect new functional material surfaces that operate through the chiral capillarity mechanism described here. Further work is currently in progress to characterize a water-based surface actuation mechanism through the interaction of anisotropic interfacial tension and chirality changes through hydration.

# Appendix A

## Cahn–Hoffman capillarity vector thermodynamics for CLC interfaces

The purpose of this Appendix is to derive the Cahn–Hoffman capillarity vector formulations for CLC interfaces. The nematic capillarity vector is defined by the gradient of the scalar field $r\gamma$:[36]

$$\xi(\mathbf{n},\mathbf{k}) = \nabla[r\gamma(\mathbf{k})], \tag{A1}$$

where $r$ is the magnitude of surface position vector $\mathbf{r}$: $\mathbf{r} = r\mathbf{k}$. Noting that $d(r\gamma) = \nabla(r\gamma)d\mathbf{r}$, the gradient of $r\gamma$ yield:

$$\xi(\mathbf{n},\mathbf{k}) = \nabla[r\gamma(\mathbf{k})] = \gamma\frac{\partial r}{\partial \mathbf{r}} + r\frac{d\gamma}{d\mathbf{r}}\gamma\mathbf{k} + \mathbf{I}_s \cdot \frac{d\gamma}{d\mathbf{k}} \tag{A2}$$

Thus, the normal and tangential components of capillarity vector for CLC interfaces are:

$$\xi_\perp(\mathbf{n},\mathbf{k}) = \gamma\mathbf{k}$$
$$\xi_\parallel(\mathbf{n},\mathbf{k}) = \mathbf{I}_s \cdot \frac{d\gamma}{d\mathbf{k}} = (\mathbf{I}_s \cdot \mathbf{n})\frac{d\gamma}{d(\mathbf{n}\cdot\mathbf{k})} = \gamma'\mathbf{n}_\parallel, \tag{A3}$$

where $\gamma' = \dfrac{d\gamma}{d(\mathbf{n}\cdot\mathbf{k})}$ and $\mathbf{n}_{||} = \mathbf{I}_s \cdot \mathbf{n}$ is the tangential component of the surface director field. Noticing that $\mathbf{I}_s$ is the $2 \times 2$ unit surface dyadic: $\mathbf{I}_s = \mathbf{I} - \mathbf{kk}$, where $\mathbf{I}$ is the $3 \times 3$ volumetric unit tensor, we have

$$\xi_\parallel(\mathbf{n},\mathbf{k}) = \mathbf{I}_s \cdot \frac{d\gamma}{d\mathbf{k}} = (\mathbf{I} - \mathbf{kk}) \cdot \frac{d\gamma}{d\mathbf{k}} = \mathbf{I} \cdot \frac{d\gamma}{d\mathbf{k}} - \mathbf{kk} \cdot \frac{d\gamma}{d\mathbf{k}} \tag{A4}$$

Using the Rapini–Papoular surface free energy $\gamma = \gamma_0 + \dfrac{W}{2}(\mathbf{n}\cdot\mathbf{k})^2$,[29] we get

$$\frac{d\gamma}{d\mathbf{k}} = W(\mathbf{n}\cdot\mathbf{k})\mathbf{n} \tag{A5}$$

Substituting eqn (A5), we obtain the tangential component of the capillarity vector:

$$\xi_\parallel(\mathbf{n},\mathbf{k}) = W(\mathbf{n}\cdot\mathbf{k})\mathbf{n} - W(\mathbf{n}\cdot\mathbf{k})^2\mathbf{k} = W(\mathbf{n}\cdot\mathbf{k})(\mathbf{n} - (\mathbf{n}\cdot\mathbf{k})\mathbf{k}) \tag{A6}$$

Hence, the total capillary pressure $p_c$ is defined by $p_c = \nabla_s \cdot \xi$, the divergence of the capillary vector follows the rule[28]

$$p_c = \nabla_s \cdot \xi = \nabla_s \cdot (\xi_\parallel + \xi_\perp)$$
$$= \underbrace{\frac{\partial \xi_\perp}{\partial \mathbf{k}} : (\nabla_s \mathbf{k})}_{\text{area size change}} + \underbrace{\frac{\partial \xi_\parallel}{\partial \mathbf{k}} : (\nabla_s \mathbf{k})}_{\text{area rotation}} + \underbrace{\frac{\partial \xi_\parallel}{\partial \mathbf{n}} : \nabla_s \mathbf{n}}_{\text{director curvature}} \tag{A7}$$

Using eqn (A3), the contribution from the normal component $\xi_\perp$, the area size change contribution becomes

$$\frac{\partial \xi_\perp}{\partial \mathbf{k}} : \nabla_s \mathbf{k} = \gamma\mathbf{I}_s : \nabla_s \mathbf{k} = -\gamma\kappa, \tag{A8}$$

where $\nabla_s \mathbf{k} = -\kappa \mathbf{tt}$. According to eqn (A6), the area rotation contribution becomes

$$\frac{\partial \xi_\parallel}{\partial \mathbf{k}} : (\nabla_s \mathbf{k}) = -W\left((\mathbf{n}\cdot\mathbf{t})^2 - (\mathbf{n}\cdot\mathbf{k})^2\right)\kappa. \tag{A9}$$

The director curvature contribution is determined using eqn (A6), to obtain:

$$\frac{\partial \xi_\parallel}{\partial \mathbf{n}} = \frac{\partial}{\partial \mathbf{n}}\left(W(\mathbf{n}\cdot\mathbf{k})(\mathbf{n} - (\mathbf{n}\cdot\mathbf{k})\mathbf{k})\right)$$
$$= W\mathbf{kn} - 2W(\mathbf{k}\times\mathbf{n})\mathbf{kk} + W(\mathbf{n}\cdot\mathbf{k})\mathbf{I} \tag{A10a}$$

$$\frac{\partial \xi_\parallel}{\partial \mathbf{n}} : \nabla_s \mathbf{n} = \frac{\partial \xi_\parallel}{\partial \mathbf{n}} : \mathbf{t}\frac{\partial \mathbf{n}}{\partial s} = W(\mathbf{t}\cdot\mathbf{n})\left(\mathbf{k}\cdot\frac{\partial \mathbf{n}}{\partial s}\right) + W(\mathbf{n}\cdot\mathbf{k})\left(\mathbf{t}\cdot\frac{\partial \mathbf{n}}{\partial s}\right) \tag{A10b}$$

# Appendix B

## Director curvature pressure

The purpose of this Appendix is (i) to derive a general expression of the director curvature pressure $p_N$, (ii) to determine generic sufficient conditions, under which $p_N = 0$, and (iii) to use (i) and (ii) to show that for a planar surface with a uniform tangential helix vector $p_N = 0$ and no surface wrinkling can be observed as predicted by ref. 23a, using other approaches.

**General expression for the director curvature pressure ($p_N$).** Using eqn (8), the director curvature contribution to the capillary pressure, $p_N$ appears due to orientation gradients:

$$p_N = \frac{\partial \xi_\parallel}{\partial \mathbf{n}} : \nabla_s \mathbf{n} \tag{B1a}$$

$$p_N = W((\mathbf{k}\cdot\mathbf{n})(\nabla_s \cdot \mathbf{n}) + \mathbf{kn}:\nabla_s \mathbf{n}). \tag{B1b}$$

To further analyse this expression, we need the covariant surface gradient of the director field $\nabla_s \mathbf{n}$ (for details see ref. 47):

$$\nabla_s \mathbf{n} = \mathbf{a}^\alpha \mathbf{n}_{,\alpha} = (n_{\beta;\alpha} - b_{\beta\alpha}n_\perp)\mathbf{a}^\alpha\mathbf{a}^\beta + (n_{\perp,\alpha} + b_{\beta\alpha}n^\beta)\mathbf{a}^\alpha\mathbf{k}$$
$$= (n_{\beta;\alpha}\mathbf{a}^\alpha\mathbf{a}^\beta - n_\perp\mathbf{b}) + (\nabla_s n_\perp + \mathbf{b}\cdot\mathbf{n})\mathbf{k} \tag{B2}$$

where a semicolon denotes covariant differentiation, $\mathbf{a}_\alpha$ are the two tangential base vectors, $\mathbf{a}^\alpha$ are the two reciprocal base vectors, the director field is $\mathbf{n} = n_\beta\mathbf{a}^\beta + n_\perp\mathbf{k}$, and the curvature tensor $\mathbf{b}$ is

$$\mathbf{b} = -\frac{\partial \mathbf{k}}{\partial \mathbf{R}} = -\nabla_s \mathbf{k}, \quad \nabla_s(*) = \mathbf{I}_s \cdot \nabla_s(*) = \frac{\partial(*)}{\partial \mathbf{R}} = \mathbf{a}^\alpha\frac{\partial(*)}{\partial u^\alpha} \tag{B3}$$

where $\mathbf{R}$ is the position vector given parametrically by $\mathbf{R} = \mathbf{R}(u^\alpha)$, $\alpha = 1$, 2 and $u^\alpha$ are the surface coordinates. The average curvature $H$ and the Gaussian or total curvature $\kappa$ are

$$2H = \mathbf{I}_s : \mathbf{b} = -\nabla_s \cdot \mathbf{k} = -\mathbf{a}^\alpha\frac{\partial \mathbf{k}}{\partial u^\alpha} = b_\alpha{}^\alpha = (c_1 + c_2) \tag{B4}$$

$$K = -\frac{1}{2}\varepsilon_s : \left(\mathbf{b}\cdot\varepsilon_s\cdot\mathbf{b}\right) = \frac{1}{2}\varepsilon^{\alpha\beta}\varepsilon^{\gamma\delta}b_{\alpha\gamma}b_{\beta\delta} = (c_1c_2) \tag{B5}$$

where $c_1$ and $c_2$ are the radius of curvature, and $\varepsilon_s$ is the dyadic surface unit alternator:

$$\begin{aligned}\boldsymbol{\varepsilon}_s &= -\mathbf{k} \times \mathbf{I}_s = -\mathbf{I}_s \times \mathbf{k} = -\mathbf{k} \times \mathbf{I} = -\mathbf{I} \times \mathbf{k} \\ &= \mathbf{a}^\alpha \mathbf{a}^\beta \varepsilon_{\alpha\beta} = \mathbf{a}_\alpha \mathbf{a}_\beta \varepsilon^{\alpha\beta}\end{aligned} \quad (\text{B6})$$

The surface director gradient $\nabla_s \mathbf{n}$ can then be decomposed into the $2 \times 2$ symmetric surface gradient tensor $\mathbf{A}$, the $2 \times 2$ antisymmetric surface gradient tensor $\mathbf{W}$, and the $2 \times 1$ surface gradient tensor $\mathbf{R}$:

$$\nabla_s \mathbf{n} = \mathbf{A} + \mathbf{W} + \mathbf{R} \quad (\text{B7a})$$

$$\begin{aligned}\mathbf{A} &= A_{\alpha\beta} \mathbf{a}^\alpha \mathbf{a}^\beta; \\ A_{\alpha\beta} &= A_{\beta\alpha} = n_{(\beta;\alpha)} - n_\perp b_{\alpha\beta}; \; n_{(\beta;\alpha)} = \frac{1}{2}(n_{\beta;\alpha} + n_{\alpha;\beta})\end{aligned} \quad (\text{B7b})$$

$$\begin{aligned}\mathbf{W} &= W_{\alpha\beta} \mathbf{a}^\alpha \mathbf{a}^\beta; \\ W_{\alpha\beta} &= -W_{\beta\alpha} = n_{[\beta;\alpha]}; \; n_{[\beta;\alpha]} = \frac{1}{2}(n_{\beta;\alpha} - n_{\alpha;\beta})\end{aligned} \quad (\text{B7c})$$

$$\mathbf{R} = R_{\alpha n} \mathbf{a}^\alpha \mathbf{k}; R_{\alpha n} = n_{\perp,\alpha} + b_{\alpha\beta} n^\beta \quad (\text{B7d})$$

In addition, the surface divergence of the director is determined from eqn (B2) to be

$$\nabla_s \mathbf{n} = \mathbf{a}^\alpha \mathbf{n}_{,\alpha} = (n_{\beta;\alpha} - b_{\beta\alpha} n_\perp) \mathbf{a}^\alpha \mathbf{a}^\beta = \mathbf{I}_s{:}\mathbf{A} = n_{\alpha;\alpha} - 2Hn_\perp \quad (\text{B8})$$

Replacing eqn (B7a–B8) into eqn (B1b) we determine a general and detailed expression for the director pressure in terms of director component $(n_\alpha, n_{\alpha:\alpha}, n_\perp, n_\parallel)$ and curvatures $(H, b_{\alpha,\beta})$:

$$\begin{aligned}p_N &= W((\mathbf{n}\cdot\mathbf{k})\mathbf{I}_s{:}\mathbf{A} + \mathbf{n}\cdot\mathbf{R}\cdot\mathbf{k}) \\ &= W((n_{(\alpha;\alpha)} - 2n_\perp H)n_\perp + (n_{\perp,\alpha} + b_{\alpha\beta}n^\beta)n_\alpha)\end{aligned} \quad (\text{B9})$$

**Vanishing director curvature pressure ($p_N = 0$).** Herein, we analyse some likely cases of $p_N = 0$ for (a) 2D surfaces and then (b) 1D planar lines.

(a) For flat surfaces, eqn (B9), it simplifies to

$$p_N(\mathbf{b} = \mathbf{0}) = W(n_{(\alpha;\alpha)}n_\perp + \mathbf{n}\cdot\mathbf{a}^\alpha n_{\perp,\alpha}) \quad (\text{B10})$$

If the director field is homeotropic, $n_{(\alpha;\alpha)} = \mathbf{n}\cdot\mathbf{a}^\alpha = 0$, and $p_N = 0$. If the director is tangential, $n_{\perp,\alpha} = n_\perp = 0$, and $p_N = 0$.

(a) For 1D planar lines, the director pressure is:

$$p_N = W(\mathbf{t}\cdot\mathbf{n})\left(\mathbf{k}\cdot\frac{\partial\mathbf{n}}{\partial s}\right) + W(\mathbf{n}\cdot\mathbf{k})\left(\mathbf{t}\cdot\frac{\partial\mathbf{n}}{\partial s}\right), \quad (\text{B11})$$
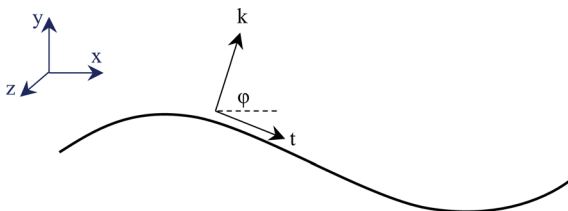


**Fig. 10** Geometry of the free surface, unit normal $\mathbf{k}$, normal angle $\varphi$, unit tangent $\mathbf{t}$, and the $(x, y, z)$ coordinate system.

where $\mathbf{t}$ is the unit tangent, $\mathbf{k}$ the unit normal, and $s$ the arc-length. For homeotropic and planar straight lines, we find $p_N = 0$. For straight lines with line gradients, using rectangular $(x, y, z)$ coordinates with unit vectors $(\delta_x = t, \delta_y = \mathbf{k}, \delta_z)$ and a director-filed $\mathbf{n} = n_x\delta_x + n_y\delta_y + n_z\delta_z$, the pressure equation (eqn (B11)) becomes

$$p_N = W(n_y n_{x,x} + n_x n_{y,x}), \quad (\text{B12})$$

which vanishes when $n_x n_y = C = $ constant. Hence, under planar or homeotropic orientation, there is no director pressure. Using the unit length of the director $\mathbf{n}\cdot\mathbf{n} = 1$, no director pressure is generated for the director field, satisfying

$$n_y{}^4 + n_z{}^2 n_y{}^2 - n_y{}^2 + c^2 = 0. \quad (\text{B13})$$

**Proof of zero director curvature pressure for planar surfaces ($H = 0$) with tangential cholesteric helix ($\mathbf{h} = \mathbf{t}$).** When the cholesteric helix is tangential to the straight line then

$$\mathbf{s} = x, \quad \mathbf{t} = \delta_x = \text{constant}, \quad \delta_x\cdot\mathbf{n} = 0, \quad \delta_x\cdot\left(\frac{d\mathbf{n}}{dx}\right) = 0.$$

Using eqn (B10) we find

$$p_N = W\left\{(\delta_y\cdot\mathbf{n})\underbrace{\left(\delta_x\cdot\frac{d\mathbf{n}}{dx}\right)}_{=0} + (\delta_x\cdot\mathbf{n})\underbrace{\left(\delta_y\cdot\frac{d\mathbf{n}}{dx}\right)}_{=0}\right\} = 0. \quad (\text{B14})$$

No director pressure is generated because the director gradients and the director components have no projection on the $x$-axis.

# Appendix C

### Derivation of shape and normal angle equations

The purpose of this Appendix is to formulate the capillary shape equation for the splay-bend director.

The geometry of the free interface is characterized by a cylindrical surface such that its curvature in the $z$-direction is zero and focused on the projection $\mathbf{x}(s)$ in the $x$–$y$ plane (Fig. 10). The unit tangent $\mathbf{t}$ and the unit normal $N$ to the surface are given by

$$\mathbf{t}(s) = \frac{\partial\mathbf{x}(s)}{\partial s}; \frac{\partial\mathbf{t}(s)}{\partial s} \equiv \frac{\partial^2\mathbf{x}(s)}{\partial s^2} = \kappa\mathbf{k}(s), \quad (\text{C1})$$

where $\kappa$ is the curvature, quantifying the deviation from linearity.

Because $\mathbf{t}$ is a unit vector, it can be expressed with the normal angle: $\mathbf{t}(x) = (\sin\varphi(x), -\cos\varphi(x), 0)$. In the normal angle parameterization, the curvature is: $\kappa = \dfrac{d\varphi}{ds}$. Using the definition: $\dfrac{dx}{ds} = \sin\varphi$, the director curvature pressure is $\dfrac{d\mathbf{n}}{ds} = \dfrac{d\mathbf{n}}{dx}\dfrac{dx}{ds} = \dfrac{d\mathbf{n}}{dx}\sin\varphi$, and $\kappa = \dfrac{d\varphi}{dx}\sin\varphi$. By substituting $\kappa$ and $\dfrac{d\mathbf{n}}{ds}$ in eqn (5), the shape equation becomes

$$\frac{p_c}{\gamma_o} = \left\{ \left(1 - \frac{B}{2}(\mathbf{n}\cdot\mathbf{k})^2 + B(\mathbf{n}\cdot\mathbf{t})^2\right)\sin\phi \right\}\frac{\mathrm{d}\phi}{\mathrm{d}x} - \left\{ B(\mathbf{k}\cdot\mathbf{n})\left(\frac{\mathrm{d}\mathbf{n}}{\mathrm{d}x}\cdot\mathbf{t}\right) \right.$$
$$\left. + B(\mathbf{n}\cdot\mathbf{t})\left(\frac{\mathrm{d}\mathbf{n}}{\mathrm{d}x}\cdot\mathbf{k}\right) \right\}\sin\phi. \tag{C2}$$

Setting $p_c = 0$ and using the splay-bend director distribution $\mathbf{n}(x)$: $\mathbf{n}(x) = (\cos qx, \sin qx, 0)$ and surface unit normal $\mathbf{k}(x)$: $\mathbf{k}(x) = (\cos\varphi(x), \sin\varphi(x), 0)$, gives the governing nonlinear first-order ODE for the normal angle $\varphi(x, B, q)$:

$$\frac{\mathrm{d}\varphi}{\mathrm{d}x} = \frac{q_0 B\sin(\varphi)\left\{\sin^2(\varphi - q_0 x) - \cos^2(\varphi - q_0 x)\right\}}{\sin(\varphi)\left\{1 - \frac{B}{2}\cos^2(\varphi - q_0 x) + B\sin^2(\varphi - q_0 x)\right\}}. \tag{C3}$$

## Acknowledgements

## References

1 P.-G. d. Gennes and J. Prost, *The physics of liquid crystals*, Clarendon Press;Oxford University Press, Oxford New York, 2nd edn, 1995, p xvi, 597 p.

2 A. C. Neville, *Biology of fibrous composites: development beyond the cell membrane*, Cambridge University Press, New York, NY, USA, 1993, p vii, 214 p.

3 A. D. Rey, E. E. Herrera-Valencia and Y. K. Murugesan, Structure and dynamics of biological liquid crystals, *Liq. Cryst.*, 2014, **41**(3), 430–451.

4 (a) Y. Bouligand, Twisted Fibrous Arrangements in Biological-Materials and Cholesteric Mesophases, *Tissue Cell*, 1972, **4**(2), 189–217; (b) G. De Luca and A. D. Rey, Chiral front propagation in liquid-crystalline materials: Formation of the planar monodomain twisted plywood architecture of biological fibrous composites, *Phys. Rev. E: Stat., Nonlinear, Soft Matter Phys.*, 2004, **69**(1), 011706; (c) G. De Luca and A. D. Rey, Monodomain and polydomain helicoids in chiral liquid-crystalline phases and their biological analogues, *Eur. Phys. J. E: Soft Matter Biol. Phys.*, 2003, **12**(2), 291–302; (d) A. D. Rey and E. E. Herrera-Valencia, Liquid crystal models of biological materials and silk spinning, *Biopolymers*, 2012, **97**(6), 374–396.

5 F. Livolant and A. Leforestier, Condensed phases of DNA: Structures and phase transitions, *Prog. Polym. Sci.*, 1996, **21**(6), 1115–1164.

6 E. Belamie, G. Mosser, F. Gobeaux and M. M. Giraud-Guille, Possible transient liquid crystal phase during the laying out

of connective tissues: alpha-chitin and collagen as models, *J. Phys.: Condens. Matter*, 2006, **18**(13), 115–129.

7 M. M. GiraudGuille, Twisted Plywood Architecture of Collagen Fibrils in Human Compact-Bone Osteons, *Calcif. Tissue Int.*, 1988, **42**(3), 167–180.

8 A. D. Rey, Liquid crystal models of biological materials and processes, *Soft Matter*, 2010, **6**(15), 3402–3429.

9 I. I. Smalyukh, O. V. Zribi, J. C. Butler, O. D. Lavrentovich and G. C. L. Wong, Structure and dynamics of liquid crystalline pattern formation in drying droplets of DNA, *Phys. Rev. Lett.*, 2006, **96**(17), 177801.

10 A. F. Miller and A. M. Donald, Imaging of anisotropic cellulose suspensions using environmental scanning electron microscopy, *Biomacromolecules*, 2003, **4**(3), 510–517.

11 J. E. Kirkwood and G. G. Fuller, Liquid Crystalline Collagen: A Self-Assembled Morphology for the Orientation of Mammalian Cells, *Langmuir*, 2009, **25**(5), 3200–3206.

12 P. J. Willcox, S. P. Gido, W. Muller and D. L. Kaplan, Evidence of a cholesteric liquid crystalline phase in natural silk spinning processes, *Macromolecules*, 1996, **29**(15), 5106–5110.

13 V. Sharma, M. Crne, J. O. Park and M. Srinivasarao, Structural Origin of Circularly Polarized Iridescence in Jeweled Beetles, *Science*, 2009, **325**(5939), 449–451.

14 T. L. Tan, D. Wong and P. Lee, Iridescence of a shell of mollusk Haliotis Glabra, *Opt. Express*, 2004, **12**(20), 4847–4854.

15 S. Vignolini, E. Moyroud, B. J. Glover and U. Steiner, Analysing photonic structures in plants, *J. R. Soc., Interface*, 2013, **10**(87), 20130394.

16 G. Agez, R. Bitar and M. Mitov, Color selectivity lent to a cholesteric liquid crystal by monitoring interface-induced deformations, *Soft Matter*, 2011, **7**(6), 2841–2847.

17 H. M. Whitney, M. Kolle, P. Andrew, L. Chittka, U. Steiner and B. J. Glover, Floral Iridescence, Produced by Diffractive Optics, Acts As a Cue for Animal Pollinators, *Science*, 2009, **323**(5910), 130–133.

18 R. S. Werbowyj and D. G. Gray, Liquid-Crystalline Structure in Aqueous Hydroxypropyl Cellulose Solutions, *Mol. Cryst. Liq. Cryst.*, 1976, **34**(4), 97–103.

19 (a) H. Yoneyama, K. Kawabata, A. Tsujimoto and H. Goto, Preparation of iridescent-reflective poly(furan-co-phenylene)s by electrochemical polymerization in a cholesteric liquid crystal medium, *Electrochem. Commun.*, 2008, **10**(7), 965–969; (b) V. Arrighi, J. M. G. Cowie, P. Vaqueiro and K. A. Prior, Fine structure and optical properties of cholesteric films prepared from cellulose 4-methylphenyl urethane/\-vinyl pyrrolidinone solutions, *Macromolecules*, 2002, **35**(19), 7354–7360; (c) Y. P. Zhang, V. P. Chodavarapu, A. G. Kirk and M. P. Andrews, Structured color humidity indicator from reversible pitch tuning in self-assembled nanocrystalline cellulose films, *Sens. Actuators, B*, 2013, **176**, 692–697.

20 S. N. Fernandes, Y. Geng, S. Vignolini, B. J. Glover, A. C. Trindade, J. P. Canejo, P. L. Almeida, P. Brogueira and M. H. Godinho, Structural Color and Iridescence in

Transparent Sheared Cellulosic Films, *Macromol. Chem. Phys.*, 2013, **214**(1), 25–32.

21 (*a*) B. D. Terris, R. J. Twieg, C. Nguyen, G. Sigaud and H. T. Nguyen, Force Microscopy of Chiral Liquid-Crystal Surfaces, *Europhys. Lett.*, 1992, **19**(2), 85–90; (*b*) P. E. Cladis and M. Kleman, Cholesteric Domain Texture, *Mol. Cryst. Liq. Cryst.*, 1972, **16**(1–2), 1–20; (*c*) K. Harth, B. Schulz, C. Bahr and R. Stannarius, Atomic force microscopy of menisci of free-standing smectic films, *Soft Matter*, 2011, **7**(15), 7103–7111; (*d*) C. Zhang, S. Edo, R. Ishige, M. Tokita and J. Watanabe, Regular undulation morphology observed on fracture and film surfaces of chiral S–C* polymer, *Macromolecules*, 2008, **41**(14), 5361–5364.

22 A. D. Rey, Capillary models for liquid crystal fibers, membranes, films, and drops, *Soft Matter*, 2007, **3**(11), 1349–1368.

23 (*a*) R. Meister, H. Dumoulin, M. A. Halle and P. Pieranski, Anchoring of a cholesteric liquid crystal at the free surface, *J. Phys. II*, 1996, **6**(6), 827–844; (*b*) R. Meister, M. A. Halle, H. Dumoulin and P. Pieranski, Structure of the cholesteric focal conic domains at the free surface, *Phys. Rev. E: Stat. Phys., Plasmas, Fluids, Relat. Interdisc. Top.*, 1996, **54**(4), 3771–3782.

24 J. C. Roland, D. Reis and B. Vian, Liquid-Crystal Order and Turbulence in the Planar Twist of the Growing Plant-Cell Walls, *Tissue Cell*, 1992, **24**(3), 335–345.

25 C. T. Brett and K. Waldron, *Physiology and biochemistry of plant cell walls*, Chapman & Hall, London, 2nd edn, 1996, p xiii, 255 p.

26 (*a*) Y. K. Murugesan and A. D. Rey, Modeling Textural Processes during Self-Assembly of Plant-Based Chiral-Nematic Liquid Crystals, *Polymers*, 2010, **2**(4), 766–785; (*b*) Y. K. Murugesan and A. D. Rey, Structure and rheology of fiber-laden membranes via integration of nematodynamics and membranodynamics, *J. Non-Newtonian Fluid Mech.*, 2010, **165**(1–2), 32–44.

27 P. Rofouie, D. Pasini and A. D. Rey, Nanostructured free surfaces in plant-based plywoods driven by chiral capillarity, *Colloids Interface Sci. Commun.*, 2014, **1**, 23–26.

28 A. G. Cheong and A. D. Rey, Cahn–Hoffman capillarity vector thermodynamics for curved liquid crystal interfaces with applications to fiber instabilities, *J. Chem. Phys.*, 2002, **117**(10), 5062–5071.

29 A. Rapini and M. Papoular, Distorsion d'une lamelle nématique sous champ magnétique conditions d'ancrage aux parois, *J. Phys.*, 1969, **30**, C4–C54.

30 D. W. Hoffman and J. W. Cahn, Vector Thermodynamics for Anisotropic Surfaces .1. Fundamentals and Application to Plane Surface Junctions, *Surf. Sci.*, 1972, **31**(1), 368–388.

31 D. A. Edwards, M. Shapiro, H. Brenner and M. Shapira, Dispersion of Inert Solutes in Spatially Periodic, 2-Dimensional Model Porous-Media, *Transp. Porous Media*, 1991, **6**(4), 337–358.

32 B. I. Outram and S. J. Elston, Spontaneous and stable uniform lying helix liquid-crystal alignment, *J. Appl. Phys.*, 2013, **113**(4).

33 P. S. Salter, G. Carbone, S. A. Jewell, S. J. Elston and P. Raynes, Unwinding of the uniform lying helix structure in cholesteric liquid crystals next to a spatially uniform aligning surface, *Physical Review E*, 2009, **80**(4), 041707.

34 A. Saupe, Disclinations and Properties of Director Field in Nematic and Cholesteric Liquid-Crystals, *Mol. Cryst. Liq. Cryst.*, 1973, **21**(3–4), 211–238.

35 Y. K. Murugesan, D. Pasini and A. D. Rey, Defect textures in polygonal arrangements of cylindrical inclusions in cholesteric liquid crystal matrices, *Soft Matter*, 2013, **9**(4), 1054–1065.

36 A. G. Cheong and A. D. Rey, Cahn-Hoffman capillarity vector thermodynamics for liquid crystal interfaces, *Phys. Rev. E: Stat., Nonlinear, Soft Matter Phys.*, 2002, **66**(2), 021704.

37 A. D. Rey, Mechanical model for anisotropic curved interfaces with applications to surfactant-laden liquid-liquid crystal interfaces, *Langmuir*, 2006, **22**(1), 219–228.

38 (*a*) A. D. Rey, Nemato-capillarity theory and the orientation-induced Marangoni flow, *Liq. Cryst.*, 1999, **26**(6), 913–917; (*b*) A. D. Rey, Marangoni flow in liquid crystal interfaces, *J. Chem. Phys.*, 1999, **110**(19), 9769–9770; (*c*) R. Eelkema, M. M. Pollard, N. Katsonis, J. Vicario, D. J. Broer and B. L. Feringa, Rotational reorganization of doped cholesteric liquid crystalline films, *J. Am. Chem. Soc.*, 2006, **128**(44), 14397–14407.

39 (*a*) A. D. Rey, Generalized cholesteric permeation flows, *Phys. Rev. E: Stat., Nonlinear, Soft Matter Phys.*, 2002, **65**(2), 022701; (*b*) A. D. Rey, Simple shear and small amplitude oscillatory rectilinear shear permeation flows of cholesteric liquid crystals, *J. Rheol.*, 2002, **46**(1), 225–240; (*c*) A. D. Rey, Helix uncoiling modes of sheared cholesteric liquid crystals, *J. Chem. Phys.*, 1996, **104**(11), 4343–4346.

40 E. Doedel and B. Oldeman, *Auto-07p: Continuation and Bifurcation Software for Ordinary Differential Equations*, 2012.

41 S. Faetti and V. Palleschi, Experimental Investigation of Surface Deformations at the Nematic-Isotropic Interface - a New Method to Measure the Nehring-Saupe Elastic-Constant K-13(+), *J. Phys.*, 1985, **46**(3), 415–424.

42 O. V. Manyuhina, Shaping thin nematic films with competing boundary conditions, *Eur. Phys. J. E: Soft Matter Biol. Phys.*, 2014, **37**, 48–52.

43 A. Boudet, M. Mitov, C. Bourgerette, T. Ondarcuhu and R. Coratger, Glassy cholesteric structure: thickness variation induced by electron radiation in transmission electron microscopy investigated by atomic force microscopy, *Ultramicroscopy*, 2001, **88**(4), 219–229.

44 A. D. Rey and M. M. Denn, Analysis of Transient Periodic Textures in Nematic Polymers, *Liq. Cryst.*, 1989, **4**(4), 409–422.

45 M. Kléman and O. D. Lavrentovich, *Soft matter physics:an introduction*, Springer, New York, 2003, p xxv, 637 p., 2 p. of plates.

46 H. Maeda, An atomic force microscopy study of ordered molecular assemblies and concentric ring patterns from evaporating droplets of collagen solutions, *Langmuir*, 1999, **15**(24), 8505–8513.

47 A. D. Rey, Polar fluid model of viscoelastic membranes and interfaces, *J. Colloid Interface Sci.*, 2006, **304**(1), 226–238.